Los Alamos NATIONAL LABORATORY EST.1943

LA-UR-15-26950 (Accepted Manuscript)

Relaxation, Structure, and Properties of Semicoherent Interfaces

Shao, Shuai
Wang, Jian

Provided by the author(s) and the Los Alamos National Laboratory (2016-11-18).

To be published in: JOM

DOI to publisher's version: 10.1007/s11837-015-1691-2

Permalink to record: http://permalink.lanl.gov/object/view?what=info:lanl-repo/lareport/LA-UR-15-26950

Disclaimer:
Approved for public release. Los Alamos National Laboratory, an affirmative action/equal opportunity employer, is operated by the Los Alamos National Security, LLC for the National Nuclear Security Administration of the U.S. Department of Energy under contract DE-AC52-06NA25396. Los Alamos National Laboratory strongly supports academic freedom and a researcher's right to publish; as an institution, however, the Laboratory does not endorse the viewpoint of a publication or guarantee its technical correctness.

RESEARCH LIBRARY

Relaxation, Structure and Properties of Semi-coherent Interfaces

S. Shao[1*] and J. Wang[2]

1 - MST-8, Materials Science and Technology Division, Los Alamos National Laboratory, Los Alamos, NM 87545

2 - Mechanical and Materials Engineering, University of Nebraska-Lincoln, Lincoln, NE 68588

* - Email: sshao@lanl.gov

Abstract

Materials containing high density of interfaces are promising candidates for future energy technologies, because interfaces acting as sources, sinks, and barriers for defects can improve mechanical and irradiation properties of materials. Semi-coherent interface widely occurring in various materials is composed of a network of misfit dislocations and coherent regions separated by misfit dislocations. In this article, we review relaxation mechanisms, structure and properties of (111) semi-coherent interfaces in face centered cubic structures.

1. Introduction

Future advancements in energy technologies, such as in nuclear energy, demand novel materials that tolerate extreme environments that exceed the capability of even the most advanced materials to date [1-2]. For decades, improvements in structural materials relied heavily on processing, which, in turn, dictated resulting microstructure and properties [3]. As materials science is entering a revolutionary era, specific material properties are attained through not only the microstructure/properties of the constituents but also the control of their architecture - often with sub-micron and nanoscale dimensions [4-7]. Materials designed with high density of interfaces are among the most promising candidates. Interfaces are important in materials of any microstructural size scale, because they can act as sources, sinks, barriers, and storage sites for defects - including dislocations, which are the main carrier of plastic deformation [3]. In nanostructured materials, interfaces dominate mechanical response of materials and can engender properties superior to those of their coarse-grained counterparts [8-10].

Semi-coherent interface is a very common type of interface that is commonly found in a wide spectrum of instances, such as expitaxial layers, precipitation materials, and diffusional or diffusionless phase transformations [11]. This widespread occurrence is due to its high mechanical and thermal stability [11]. Generally, interfaces act as strong barriers to dislocations [4-5, 12-17] confining them with layers/grains. In a semi-coherent interface, a network of misfit dislocations exists and separates the coherent regions, thereby canceling the coherency strain inside the layers/grains [18-25]. The misfit dislocations provide strain concentrations and act as sources for nucleation of lattice dislocations. Therefore, semi-coherent interface has the unique ability to improve the ductility of materials while maintaining strength [8-10, 26-34]. In certain interfaces with low shear strength, such as the {111} interfaces in face centered cubic structures (FCC), the strain concentration at the dislocation cores is greatly reduced due to the core-spreading [26-28, 35]. In this case, the dislocation lines may lose the privilege as a nucleation source for lattice dislocations to the dislocation intersections (nodes). Owing to the presence of the misfit dislocation network, the semi-coherent interfaces also have superior irradiation resistance. Recent atomistic simulations combining in-situ/ex-situ TEM observations [36-42] have revealed that the misfit dislocations have superior

diffusivity for the point defects, and the nodes have very low formation energies for point defects. Such a network therefore facilitates recombination of the Frenkel pairs as well as the climb of dislocation on the interface by virtue of absorbing, emitting and transporting the point defects. Therefore semi-coherent interfaces are a superior platform for managing the point and line defects in the interface.

In this article, we review our recent work [35, 43-46] combining the atomistic simulations and defect theory to investigate the relaxation mechanism and the resulting structure of the misfit dislocation network on the semi-coherent interfaces. We summarize the mechanical property as well as the irradiation property of the interface in terms of the nucleation mechanisms of the lattice dislocations and formation energies of the vacancy and interstitials at the nodes/dislocations. The variation of the aforementioned properties has been correlated to the structural variation of the nodes.

2. Relaxation of the (111) semicoherent interface

The un-relaxed FCC (111) interfaces exhibit various local atomic structures due to the mismatch of lattice parameters between the FCC crystals straddling the interface. Fig. 1 shows the un-relaxed Cu-Ni (111) interface. A *geometry analysis approach* (Fig. 1) is adopted to characterize the structures. One of the two crystals is used as the reference in the un-relaxed structure. The local atomic structure is identified by calculating the distance from an atom in the other crystal to the closest atomic site (FCC, ISF or HESF). If the distance is smaller than a critical value, the atom is identified as the respective structure. Following the convention of Peierls-Nabarro dislocation model, the critical distance Dc is chosen to be 0.25|b|, where |b| is the length of Burgers vector of a Shockley partial dislocation. Therefore, four types of regions are characterized form the inteface: near-FCC (normal (111) stacking between the 1st Ni and 1st Cu layers, $A_{Ni}B_{Ni}C_{Cu}A_{Cu}$), near-ISF (the intrinsic stacking fault between the 1st Ni and 1st Cu layers, $A_{Ni}B_{Ni}A_{Cu}B_{Cu}$), HESF (high-energy stacking fault structure between the 1st Ni and 1st Cu layers, $A_{Ni}B_{Ni}B_{Cu}C_{Cu}$), and the region separating the former three regions. The FCC, ISF regions can be treated as a result of the introduction of Shockley partial loops (dashed red and blue circles in Fig. 1) into a coherent interface with coincidence site

lattice (HESF structure). The partial loops have Burgers vectors b_1, $-b_2$, b_3, $-b_1$, b_2, $-b_3$, where $b_1 = \frac{a}{6}[2\bar{1}\bar{1}]$, $b_2 = \frac{a}{6}[\bar{1}2\bar{1}]$ and $b_3 = \frac{a}{6}[\bar{1}\bar{1}2]$.

Each of the aforementioned atomic structures represents different excess interface potential energy. Therefore, we have performed the molecular static calculation to generate the generalized stacking fault energy (GSFE) profile of the coherent Cu-Ni (111) interface (cyan curve in Fig. 2). This profile includes the interface excess potential energies of all possible coherent interface structures. As shown, the HESF has the highest energy (933 mJ/m^2); the unstable stacking fault, which correspond to the forth region, has energy of 269 mJ/m^2. The FCC and ISF structures have the lowest energy (78 mJ/m^2 and 119 mJ/m^2, respectively), and therefore are stable. During relaxation, the interface minimizes its excess potential energy by increasing the areas with perfect and near-perfect FCC and ISF structures and hence increasing coherence. Shown in Fig. 3 is the relaxation of the Cu-Ni semi-coherent interface. Fig. 3a and 3b show the interface before and after relaxation colored by geometry analysis. It is clear that the majority of the un-relaxed interface is away from the stable configuration and only the center of the FCC and ISF regions possess the minimum structure. After relaxation, the coherence of the interface increases associated with the expansion of regions with perfect and near-perfect FCC and ISF structures (the blue/near blue regions). The region separating the FCC, ISF and HESF regions also shrinks to the misfit dislocation lines (red region in Fig. 3b). Fig. 3c and 3d show the disregistry plots [35, 43-46] around a node before and after the relaxation. The solid lines (red and blue) correspond to the Shockley partial loops. As shown, after the relaxation the Shockley partial loops have expanded and reacted with each other to form the misfit dislocation lines (dashed lines in Fig. 3d and red shaded region) with Burgers vectors $\mathbf{b}_1$, $\mathbf{b}_2$ and $\mathbf{b}_3$.

After the relaxation, the HESF regions reduced to the intersections of the misfit dislocations. It is also interesting to note from Fig. 3b that the HESF structure is virtually removed after the relaxation, and the node exhibits a “spiral pattern”. This is attributed to the relaxation mechanisms of the HESF. Fig. 4 shows the relaxation of HESF structure. To remove the high-energy structure (Fig. 4a), the interfacial Cu and Ni atoms in HESF relatively rotate (Fig. 4b), relatively dilatate/shrink (Fig. 4c), and rigidly shift against each other (Fig. 4d). The relative rotation and dilatation destroys the HESF and forms the

near FCC and ISF structure at a node. The relative dilatation also creates positive (negative) free volume in the crystal with larger (smaller) lattice. The relative rigid shift removes the HESF at the center of a node. Due to the relative rotation, a spiral pattern is present in the nodes.

It is important to note that the reduction of the interface excess potential energy cannot infinitely shrink the core size of the misfit dislocation as well as the nodes. The coherent regions of the relaxed interface are subject to uniform biaxial normal strains: the crystal with the smaller (larger) lattice parameter is under tension (compression). The lattice mismatch is then accommodated by the misfit dislocations that lie between the coherent regions. The misfit dislocations and nodes have the opposite stress states to the coherent regions – compression in the smaller lattice and tension in the larger lattice. The amplitude of the stress in the core of the misfit dislocation and nodes is dependent on the size of the core, i.e. the narrower (wide) the core, the higher (lower) the strain concentration at dislocations and nodes. Higher strain concentrations at the core also results in higher core energy of the misfit dislocations. Therefore, the relaxation of the semi-coherent interface is a completion between the reduction of the interface excess potential energy and the increase of the core strain energy associated with the formation of the misfit dislocation network.

Under loading, the GSFE profile changes. We have measured the GSFE profile of a coherent Cu-Ni (111) interface that assumes the lattice constant of Cu and Ni (Fig. 2, red and blue curves), to study the variation of GSFE when the interface is under in-plane tension and compression. When the interface is subjected to in-plane biaxial tension (compression), the excess potential energy for the HESF increases (decreases) while the energies for the FCC, ISF as well as the unstable stacking fault structures decrease (increase). Also the slop of the GSFE profile, which drives the expansion of the Shockley partial loops, increases (decreases) under this condition. Therefore, compared to the misfit dislocation network under equilibrium conditions (Fig. 5a), the core of the dislocation and nodes expands under compressive loading (Fig. 5b) and shrinks under tensile loading (Fig. 3c). Fig. 5d shows the plot of normalized Burgers vector per unit length [43] for the Cu-Ni semi-coherent interface under the various loading conditions. The variation of the core width of misfit dislocations is evident.

3. Structures and properties at nodes

As was discussed earlier, during the relaxation of the HESF regions, the relative dilatation/compression at the nodes (as illustrated by Fig. 4c) creates positive free volume in the larger lattice and negative free volume in the smaller lattice. Shown in Fig. 6 are the contour plots of the free volume distribution [46] at a node under various conditions. The dislocation structures of the nodes have been characterized using dis-registry analysis and the obtained dislocation structures are shown in Fig. 7. Under equilibrium conditions, the free volume at node on Cu side is smeared in the vicinity (Fig. 6a and 7a). The change in core size of the nodes under loading either condenses (under tension) or further smears (under compression) the free volume. Fig. 6b shows the condensed free volume at a node on Cu side of interface. The node structure (Fig. 7b) associated with the node shown in Fig. 6b is referred to as the volume-condensed node with "constricted" triangular dislocation pattern, has three jogs (green dots) connecting two sets of interfacial dislocations in two adjacent planes: Ni1-Cu1 (blue dislocation lines, between Cu and Ni crystals) and Cu1-Cu2 (green dislocation lines, between the first and second atomic planes in the Cu crystal). The concentrated free volume is regarded as the result of the close clustering of the three jogs (green dots in Fig. 7b), as each of the jogs contains certain free volume. The high strain concentration associated with the condensed free volume at the node on Cu side can be further relaxed via the climb of the jogs along the <110> (Roman-Roman in Thompson's notation) directions. The resulting structure, referred to as volume-condensed node with "expanded" triangular dislocation pattern, is given in Fig. 6c and Fig. 7c. Such dislocation structures at the node can happen due to the mechanical loading, perturbation, and absorption of interstitials. The triangular nodes can transform into an expanded hexagonal structure (Fig. 6d and 7d) when it is relaxed at a finite temperature of above 10K. This structure has been observed in the experiment. This structure, referred to as the volume-condensed node with hexagonal dislocation pattern, is formed from the triangular nodes after a series of complex dislocation reactions (detailed information in [46]). The dislocation structure of the node also involves two adjacent (111) planes (Ni1-Cu1 and Cu1-Cu2). The hexagonal dislocation pattern contains six segmental "superior dislocations" with alternating compositions. (The "superior dislocations" refers to the double-core dislocations formed by two dislocations on the

adjacent (111) slip planes.) Three of the dislocations combine perfect-partial dislocations and three others combine partial-partials dislocations. The free volume is localized in the dislocations segments with perfect-partial type (Fig. 6d). The net character of the superior dislocations is all pure edge and equivalent to a Shockley partial dislocation. When the node with spiral dislocation pattern is subjected to in-plane biaxial compression, the amplitude of the GSFE profile is considerably reduced. Therefore, the cores of the misfit dislocations and nodes expand, the spiral pattern gradually disappears and the misfit dislocation lines become aligned with <110> directions and the traces of the (111) slip planes (as shown in Fig. 6e and 7e).

As was discussed in the introduction, for interfaces such as the (111) semi-coherent interfaces, the misfit dislocations have widely spread cores and loose the ability of nucleating lattice dislocations. In this case, the nodes always represent higher stress concentrator and therefore are the primary source for the nucleation of lattice dislocations. The structure of the node therefore has significant impact on the mechanisms for lattice dislocation nucleation.

Under in-plane tension, the volume-smeared nodes with a spiral dislocation pattern (Fig. 6a) can transform into volume-condensed nodes with triangular (Fig. 6b-c) pattern. In addition, because the slope of the GSFE profiles increase under tensile loading, the equilibrium distance between the partial misfit dislocations that bound the ISF regions decreases. Therefore, under the influence of thermo fluctuation and tensile stress, the six partial dislocations near a node temporarily recombine and form three perfect dislocation segments (red shaded regions in Fig. 8a). These segments are stronger strain concentrators compared to the partial dislocations and are aligned with the <110> directions. Therefore they act as the sources for the lattice dislocations nucleation. All three sources are activated and three equivalent slip systems with Schmid factor of 0.157 are simultaneously triggered (Fig. 5c): $[\bar{1}12](\bar{1}1\bar{1})$, $[12\bar{1}](1\bar{1}\bar{1})$, and $[2\bar{1}1](\bar{1}\bar{1}1)$, or αB on the plane (α), βC on the plane (β), and γA on the plane (γ), respectively (Fig. 8d) according to Thompson's convention. After the nucleation and emission of the lattice dislocations, the residual interface dislocation dissociates to form three stair rod dislocations (Greek-Greek type dislocations in Fig. 8d). The triangular dislocation pattern also disappears after the nucleation. As was reported earlier, if the volume-condensed

node with triangular dislocation pattern is relaxed under finite temperature of above 10K, it can transform into a hexagonal pattern. Under biaxial tension, the partial misfit dislocations near nodes also temporarily recombine and form segments of perfect dislocation along <110> directions, which then serve as the nucleation source for lattice dislocations (red shaded area). Similar to the triangular node, all three sources as well as the three equivalent slip systems are activated concurrently (Fig. 8e). Three stair-rod dislocations (red arrows) are also formed as the result of the nucleation. Unlike the triangular node, the hexagonal dislocation pattern is preserved even after the nucleation. Under biaxial compression, the disappearance of the spiral pattern realigns the dislocations lines with the traces of the {111} slip planes (Fig. 6e and 7e). The dislocation lines are expected to be the primary sources of dislocation nucleation. Due to the relatively high stress concentration at the nodes [41], lattice dislocations may nucleate from the straight misfit dislocation lines near the node. As expected, our MD simulations reveal the simultaneous nucleation of six Shockley partials from all of six misfit dislocation segments near the node (Fig. 8c). After the partial dislocation loops nucleate, they propagate, react with neighboring loops and form three stair-rod dislocations (in Fig. 8f, marked in dark red).

The transformation of the nodal dislocation structure redistributes the free volume contained in the node. For instance, the volume-smeared node with spiral pattern can jump to the volume-condensed node with triangular dislocation pattern associated with the condensation of the free volume into three jogs. Such rearrangement of the free volume has significant impact on the materials irradiation properties, such as the point defect formation energies. We have measured the vacancy formation energy (VFE) on both Cu and Ni sides and self-interstitial formation energy (IFE) on Cu side in the vicinity of the nodes. Fig. 9 shows the contour plots of VFE at node on both sides of the interface. The VFE at the dislocation cores on Cu side is 1.28 eV (Fig. 9c), which is closed to the VFE in bulk Cu (1.29 eV). On Ni side, the VFE at dislocation cores is considerably less than in bulk (Fig. 9a, 1.2 eV vs 1.51 eV). Due to the hydrostatic compression on the Ni side of the dislocations and nodes, a vacancy formation is favored to happen, which lead to a lower formation energy. The VFE at nodes, while the value on Ni side is still considerably smaller than on Cu side, is significantly less than the bulk

values. For a volume-smeared node (Fig. 9a and 9c), the VFE on the Cu and Ni side is 0.95 eV and 0.54 eV, respectively. It is interesting that VFE on the Cu side is 0.34 eV lower than in the bulk although the region is under hydrostatic tension. This is because Ni atom fills in the vacancy site where a Cu atom is removed. Consequently, the elastic strain energy on the Ni side at the node will decrease. For the volume-condensed node with triangular dislocation pattern (Fig. 9b and 9d), the VFE on the Cu side is 0.67 eV when the vacancy is on the compression side of the jog (indicated by dashed ellipse). This energy is 0.28 eV lower than in the condensed node, associated with the climb of the jogs. When the vacancy is created in the center of the extrinsic stacking fault, the triangular node transforms back into the spiral node associated with a VFE of 0.47 eV. When a vacancy is created on the Ni side of the node, the node always transform back to the spiral node. The VFE in this case is 0.05 eV. The significant decrease (consistently 0.5 eV) in the VFE for the triangular node compared to the spiral one on both Cu and Ni sides is attributed to structural transformation process of the node from triangular to spiral. The triangular node has a slightly higher energy than the spiral one.

Because Ni side of the nodes is under hydrostatic compression, while the Cu side is under is under hydrostatic compression, our calculation of SIFE is only performed on the Cu side. The SIFE is computed to be −0.14 eV when a Cu atom is embedded into the center of the volume-smeared node with spiral dislocation pattern (Fig. 10a dashed circle). This is accompanied by the transformation of the node from spiral to triangular (Fig. 10b). For the triangular node, SIFE is around −0.65 eV when a Cu atom is embedded into one of three dislocation jogs (dashed circles in Fig. 10c). When three Cu atoms are simultaneously embedded into the three jogs, the average SIFE is −0.62 eV. The expanded node shrinks accompanying the absorption of Cu interstitials (Fig. 10d). The diameter of the expanded node decreases from 2.2 nm to 1.4 nm. The results imply that the expanded node can be a stronger sink for interstitials, as compared with SIFE in the condensed node, and bulk Cu (3.08 eV) and Ni (4.64 eV).

4. Discussion

Although our work reviewed here only presents the investigation of the relaxation of the Cu-Ni (111) semi-coherent interface, the approach adopted in our work to qualitatively predict the interface structures as well as interface relaxation mechanisms

discovered here is applicable to other semi-coherent interfaces as well. However, according relaxation mechanisms we discovered, the various features demonstrated by the node in the Cu-Ni interface, such as various dislocation nucleation mechanisms and different point defect formation energies associated with the various node structures, as well as the spiral pattern at nodes, are not always the case for other FCC semi-coherent interfaces. For instance, we have inspected the structures two types of interfaces: I. twist boundary in FCC single crystals (Cu, Ag and Al), II. the Cu-Ag (111) semi-coherent interface (13% lattice mismatch). We found that both nodal structural transformation and the spiral pattern disappear in the two types of interface. The twist boundaries' interface dislocations are all pure screw-type, and the nodes are subject to zero tension and compression, therefore there is not free volume created in the nodes. This removes the driving force for the nodal structural transformation associated with the redistribution of free volume. Also the atoms in the node region have already occupied near low-energy sites (i.e. FCC and ISF), therefore the spiral pattern is not necessary. On the other hand, the larger lattice mismatch between Cu and Ag dictates a much smaller interface nodal spacing (2.2 nm in Cu-Ag vs 9.5 nm in Cu-Ni). The increase in interaction energy due to the spiral pattern surpasses reduction in the self-energy of the node and dislocation. Therefore, the spiral pattern does not appear in Cu-Ag interface. In addition, the structural transformation of a node requires certain space. For instance, the volume-condensed node with triangular dislocation pattern as depicted in Fig. 6c and 7c has a diameter of 2.2 nm, which is equal to the nodal spacing in the Cu-Ag interface. In this case, the significantly high repulsion between the jogs from adjacent nodes will suppress the nodal structural transformation. Therefore, the nodal features of the semi-coherent interfaces are subject to on the node spacing, which, in turn, is ultimately dependent on the lattice mismatch and lattice rotation.

Fig. 11 summarizes the dependence of the SP feature at nodes on the character of interface dislocations and the distance between the adjacent nodes. The distance between nodes can be calculated according to Frank-Bilby theory [2-3]. The critical distance corresponding to the disappearance of the SP feature is 2.2 nm according to the triangular node structure in Cu/Ni interface. With respect to the character of interface dislocations, (111) semi-coherent interfaces in fcc crystals can be further categorized into (i) pure twist

boundary in single phase ($b_e/b = 0$, referred to as No Mismatch & Pure Twist), (ii) bi-crystal boundary in the same orientations containing ($b_e/b = 1$, referred to as Mismatch & No Twist), and (iii) mixed boundary ($0 < b_e/b < 1$, referred to as Mismatch & Twist). For type 1, nodes don't twist and expand. For type 2 interfaces with the larger lattice mismatch (such as Cu/Ag), nodes would not twist and expand. Thus, an optimized (111) semi-coherent interface (Type 3 interfaces) with respect to sink strength for point defects should exist for a given system. For example, Cu-Ni interface can be further twisted to increase the node density while retaining the SP feature at nodes (Fig. 6).

5. Conclusion

In this article, we have reviewed our previous investigation regarding the energy minimization mechanism of semi-coherent interfaces. By examining the GSFE profile of the coherent Cu-Ni interface, two stable structures (FCC and ISF, which correspond to the energy minima on the GSFE curves) and a high-energy structure are identified. Accordingly, the regions containing the stable structures can be treated as the result of the introduction of the partial dislocation loops. The minimization of the chemical potential energy at the interface expands the loop and drives their reaction with each other to form the misfit dislocations. The reduction in the chemical potential energy is achieved at the cost of the increase of core elastic energy of the misfit dislocations. Therefore, the core width of the misfit dislocation and node is dependent on the GSFE profile of the interface. On the other hand, HESF structure is destroyed by undergoing relative twist and dilatation on the two crystals on both sides of the interface, and achieves the near FCC and ISF structure. The relative rotation is responsible for the spiral pattern at nodes, and the relative dilatation is responsible for the formation of free volume at nodes. Under various conditions, the free volume at nodes is redistributed associated with the nodal structural transformation. Under equilibrium, the node assumes a dislocation pattern with smeared free volume. The free volume of this node can condense associated with the transformation to the triangular structure under tensile loading, mechanical perturbation, and addition of interstitials. The triangular node may also transform to the volume-condensed node with hexagonal dislocation pattern when the node is relaxed under a temperature higher than 10K. The various nodal dislocation structures lead to different nucleation mechanisms for lattice dislocations. Also, associated with the redistribution of

the free volume, the different nodal structures also have significantly different point defect formation energies.

Acknowledgments

S.S. and J.W. acknowledge the support provided by the U.S. Department of Energy, Office of Science, Office of Basic Energy Sciences. J.W. also acknowledges support provided by the Los Alamos National Laboratory Directed Research and Development (LDRD-ER20140450). J.W. also acknowledges the Start-up provided by the University of Nebraska-Lincoln. The valuable discussion with Prof. A. Misra, I.J. Beyerlein, J.P. Hirth, Richard G. Hoagland, and Robert Pond is appreciated.

References

[1] Y. Chen, E.G. Fu, K.Y. Yu, M. Song, Y. Liu, Y.Q. Wang, H. Wang, and X. Zhang, *J. Mater. Res.* 30, 1300 (2015).
[2] Y. Chen, K.Y. Yu, Y. Liu, S. Shao, H. Wang, M.A. Kirk, J. Wang, and X. Zhang, *Nat. Commun.* 6, 7036 (2015).
[3] George E. Dieter, *Mechanical Metallurgy*, 3rd ed. (New York, NY: McGraw-Hill Book Co., 1976).
[4] A. Misra, J.P. Hirth, and R.G. Hoagland, *Acta Mater.* 53, 4817 (2005).
[5] J. Wang and Misra, *Curr. Opin. Solid State Mater. Sci.* 18, 19 (2014).
[6] Y. Liu, D. Bufford, H. Wang, C. Sun, and X. Zhang, *Acta Mater.* 59, 1924 (2011).
[7] A. Misra, J.P. Hirth, and H. Kung, *Philos. Mag.* 82, 2935 (2002).
[8] R.F. Zhang, J. Wang, I.J. Beyerlein, and T.C. Germann, *Scripta Mater.* 65, 1022 (2011).
[9] R.F. Zhang, J. Wang, I.J. Beyerlein, A. Misra, and T.C. Germann, *Acta Mater.* 60, 2855 (2012).
[10] J. Wang, C.Z. Zhou, I.J. Beyerlein, and S. Shao, *JOM* 66, 102 (2014).
[11] J.M. Howe, R.C. Pond, and J.P. Hirth, *Prog. Mater. Sci.* 54, 792 (2009).
[12] N. Li, J. Wang, A. Misra, and J.Y. Huang, *Microsc. Microanal.* 18, 1155 (2012).
[13] P.M. Anderson, T. Foecke, and P.M. Hazzledine, *MRS Bull. 24*, 27 (1999).
[14] Q. Li and P.M. Anderson, *Acta Mater.* 53, 1121 (2005).
[15] J.S. Carpenter, A. Misra, and P.M. Anderson, *Acta Mater.* 60, 2625 (2012).
[16] S. Shao, H.M. Zbib, I. Mastorakos, and D.F. Bahr, *J. Eng. Mater. Tech.* 135, 021001 (2013).
[17] S. Shao, H.M. Zbib, I. Mastorakos, and D.F. Bahr, *J. App. Phys.* 112, 044307 (2012).
[18] F.C. Frank, *Acta Metal.*1, 15-21 (1953).
[19] B.A. Bilby, R. Bullough, and E. Smith, *Proc. R. Soc. London A* 231, 263 (1955).
[20] R. Bullough, *Philos. Mag.* 12, 1139 (1965).
[21] J.P. Hirth and R.W. Balluffi, *Acta Metal.* 21, 929 (1973).

[22] R.C. Pond and D.S. Vlachavas, *Proc. R. Soc. London A* 386, 95 (1983).
[23] D. Mitlin, A. Misra, T.E. Mitchell, J.P. Hirth, and R.G. Hoagland, *Philos. Mag.* 85, 3379 (2004).
[24] Y. Liu, D. Bufford, S. Rios, H. Wang, J. Chen, J.Y. Zhang, X. Zhang, *J. App. Phys.* 111, 073526 (2012).
[25] J.P. Hirth, R.C. Pond, R.G. Hoagland, X.Y. Liu, and J. Wang, *Prog. Mater. Sci.* 58, 749 (2013).
[26] J. Wang, R.G. Hoagland, X.Y. Liu, A. Misra, *Acta Mater.* 59, 3164 (2011).
[27] J. Wang, R.G. Hoagland, J.P. Hirth, A. Misra, *Acta Mater.* 56, 3109 (2008).
[28] J. Wang, R.G. Hoagland, J.P. Hirth, A. Misra, *Acta Mater.* 56, 5685 (2008).
[29] A. Misra, M.J. Demkowicz, J. Wang, and R.G. Hoagland, *JOM* 60, 39 (2008).
[30] P.M. Anderson and Z. Li, *Mater. Sci. Eng. A* 319-321, 182 (2001).
[31] Y. Shen and P.M. Anderson, *J. Mech. Phys. Solids* 55, 956 (2007).
[32] J. Wang, R.F. Zhang, C.Z. Zhou, I.J. Beyerlein, and A. Misra, *Int. J. Plast. 53*, 40 (2014).
[33] I.J. Beyerlein, J. Wang, R.F. Zhang, *APL Mater.*1, 032112 (2013).
[34] I.J. Beyerlein, J. Wang, R.F. Zhang, *Acta Mater.* 61, 7488 (2013).
[35] S. Shao, J. Wang, A. Misra, and R.G. Hoagland, *Sci. Rep.* 3, 2448 (2013).
[36] Z.F. Di, X.M. Bai, Q.M. Wei, J.H. Won, R.G. Hoagland, Y.Q. Wang, A. Misra, B.P. Uberuaga, and M. Nastasi, *Phys. Rev. B* 84, 052101 (2011).
[37] N. Li, J. Wang, Y.Q. Wang, Y. Serruyz, M. Nastasi, and A. Misra, *J. App. Phys.113*, 023508 (2013).
[38] M. Rose, A.G Balogh, and H. Hahn, *Nuc. Instr. Meth. Phys. Res. B* 127/128, 119 (1997).
[39] Y. Chimi, A. Iwase, N. Ishikawa, M. Kobiyama, T. Inami, and S. Okuda, *J. Nuc. Mater.* 297, 355 (2001).
[40] E. Martínez and A. Caro, *Phys. Rev. B* 86, 214109 (2012).
[41] E. Martínez, J.P. Hirth, M. Nastasi, and A. Caro, *Phys. Rev. B* 85, 060101(R) (2012).
[42] K. Kolluri and M.J. Demkowicz, *Phys. Rev. B* 85, 205416 (2012).
[43] S. Shao, J. Wang, and A. Misra, *J. App. Phys.* 116, 023508 (2014).
[44] I. Salehinia, S. Shao, J. Wang, and H.M. Zbib, *Acat Mater.* 86, 331 (2015).
[45] S. Shao, J. Wang, A. Misra, and R.G. Hoagland *Mater. Sci. For.* 783-786, 515 (2014).
[46] S. Shao, J. Wang, I.J Beyerlein and A. Misra, *Acat Mater.* 98, 206 (2015).

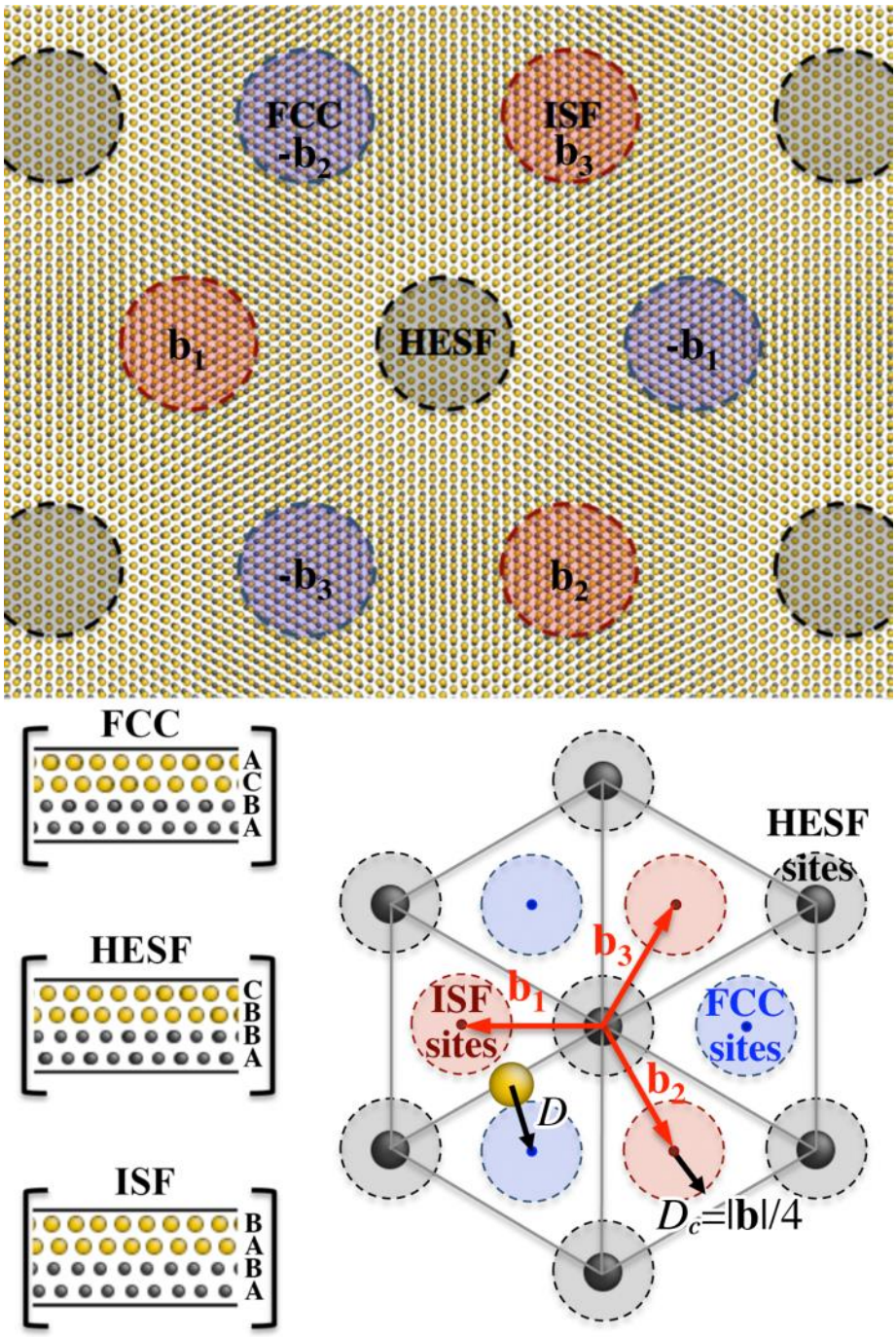

Figure 1. Geometrical feature of FCC (111) interface, showing HESF, ISF, and FCC regions that are defined according to geometry.

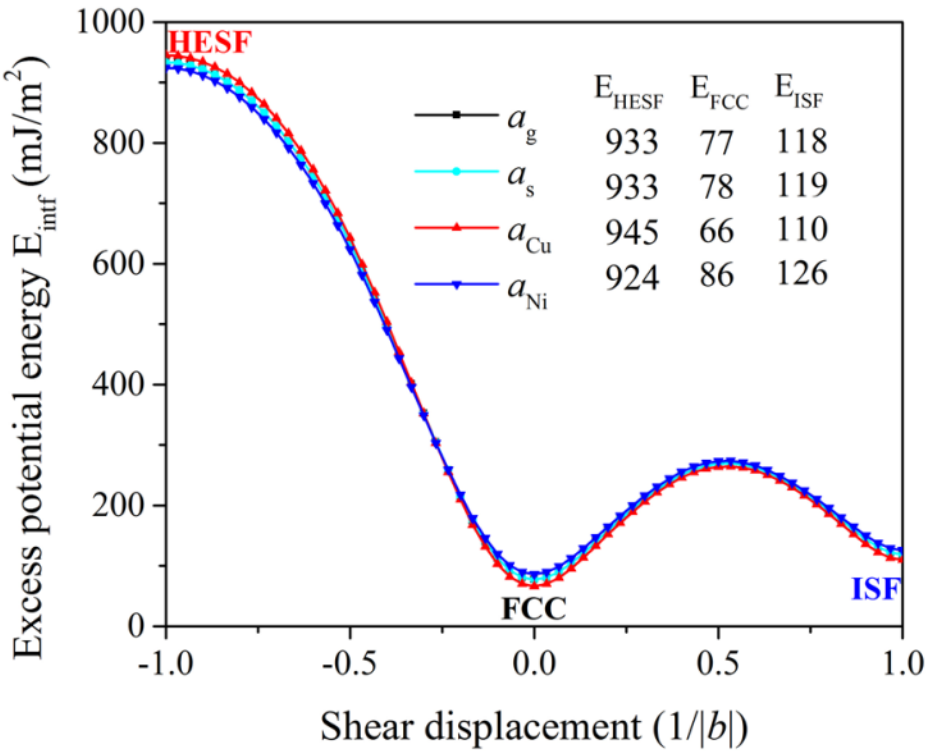

Figure 2. Excess potential energies of coherent Cu-Ni interface as a function of shear displacement along <112>direction with respect to different coherent lattices a_g, a_s, a_{Cu}, and a_{Ni}, $|b|$ is the magnitude of Burgers vector of a Shockley partial dislocation.

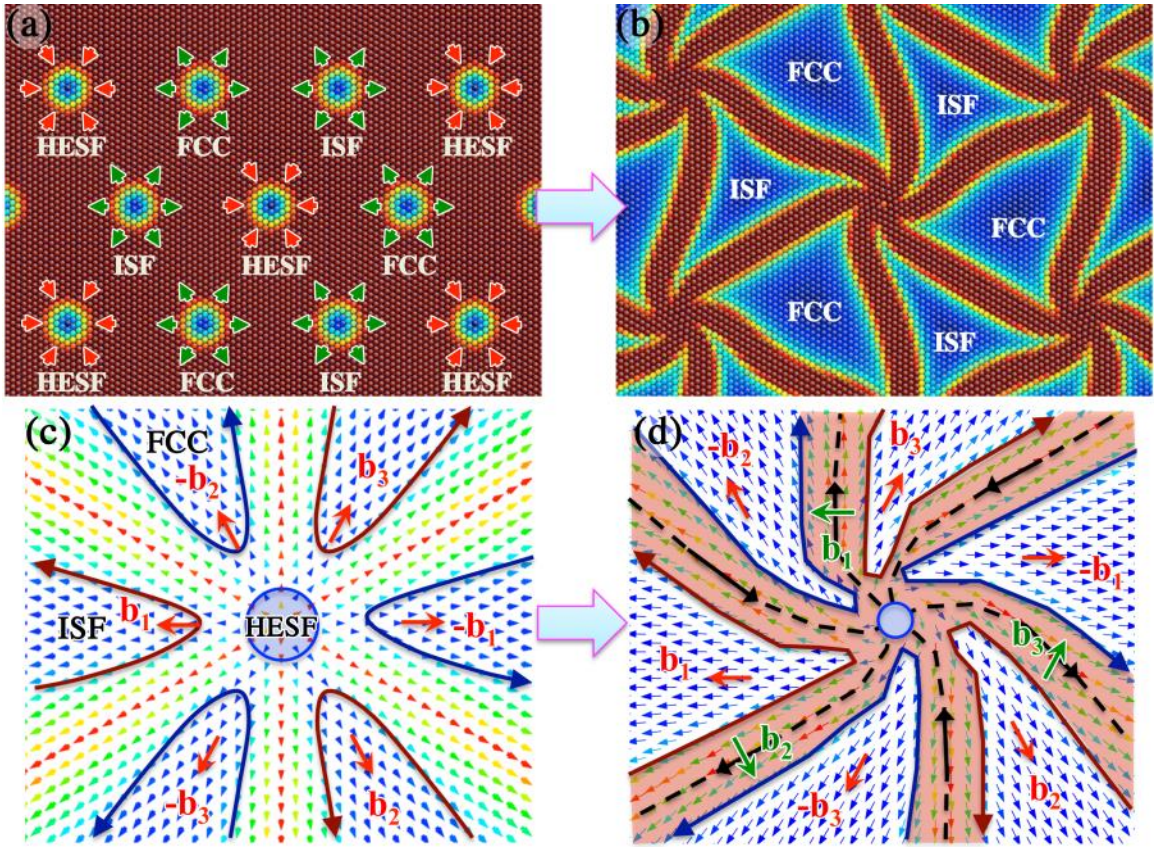

Figure 3. (a) Atomistic structure of the un-relaxed Cu-Ni interface showing three regions, FCC, ISF, and HESF according to stacking sequence determined by geometry analysis. (b) Atomistic structure of the relaxed Cu-Ni interface showing curved dislocation lines, nodes, and two regions ISF and FCC according to geometry analysis. The red regions indicate misfit dislocation lines. (c) and (d) The disregistry plots of the un-relaxed and relaxed Cu-Ni interfaces, showing Burgers vectors associated with the FCC and ISF regions. The partial loops associated with the FCC and ISF regions are denoted using solid lines and the dashed lines in (d) indicate the six partial dislocation segments. The arrows on the solid and dashed lines indicate the sense of dislocation lines.

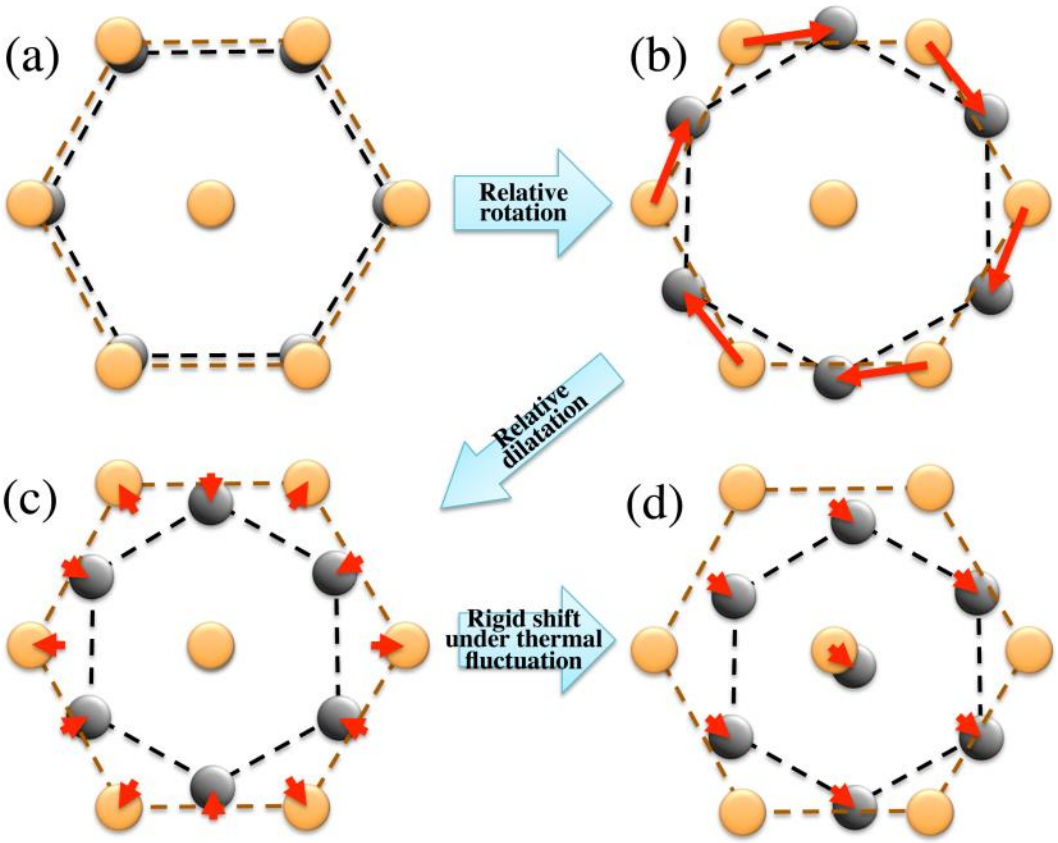

Figure 4. Relaxation mechanisms of a HESF structure, showing (a) un-relaxed HESF structure, (b) local rotation across the interface plane, (c) subsequent dilation and shrink, and (d) slight shift of the center atom.

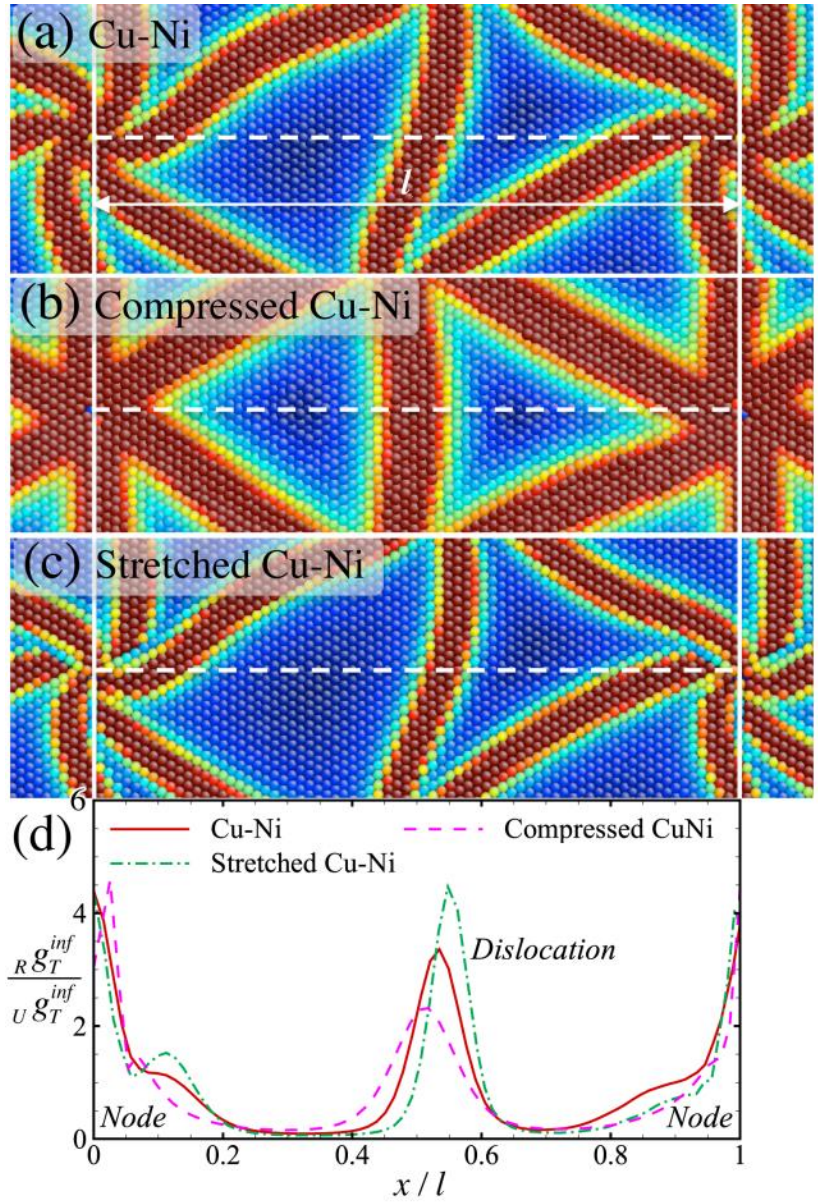

Figure 5. Variation of dislocation core width in Cu-Ni semi-coherent interface with respect to biaxial loading, (a) zero applied stress, (b) biaxial compression, and (c) biaxial tension. (d) The normalized Burgers vector per unit length along <112> direction.

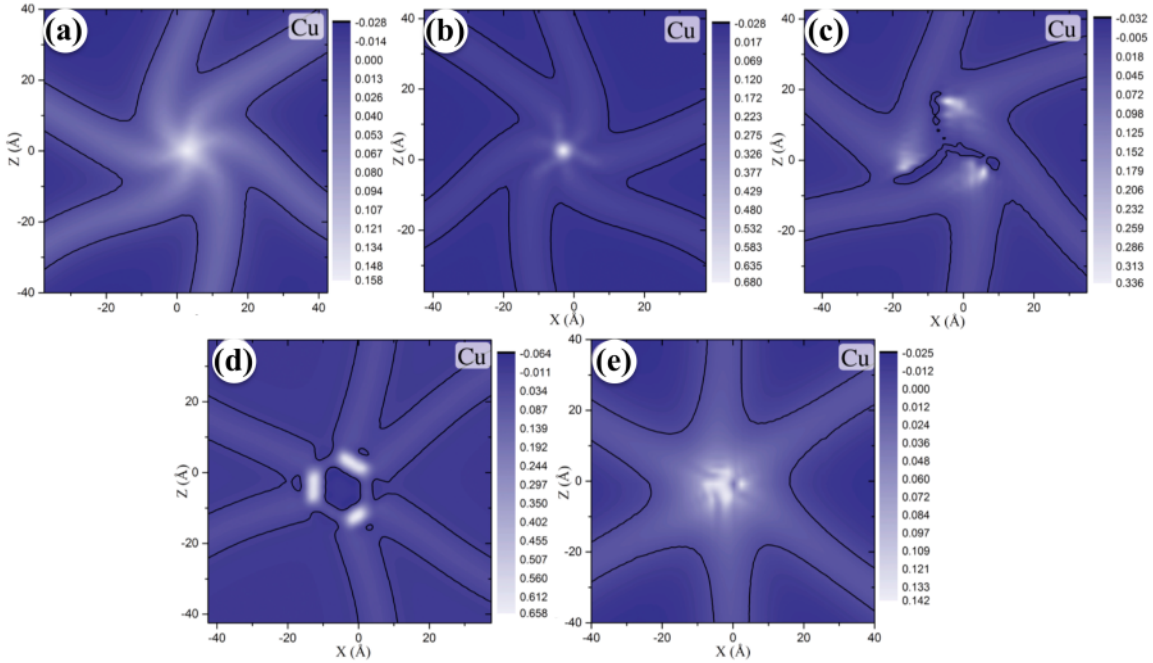

Figure 6. Contour plot of free volume of (a) volume smeared node with spiral dislocation pattern, (b) volume condensed node with "constricted" triangular dislocation pattern, (c) volume condensed node with "expanded" triangular dislocation pattern, (d) volume condensed node with hexagonal dislocation pattern, (e) volume smeared node with straight dislocation pattern.

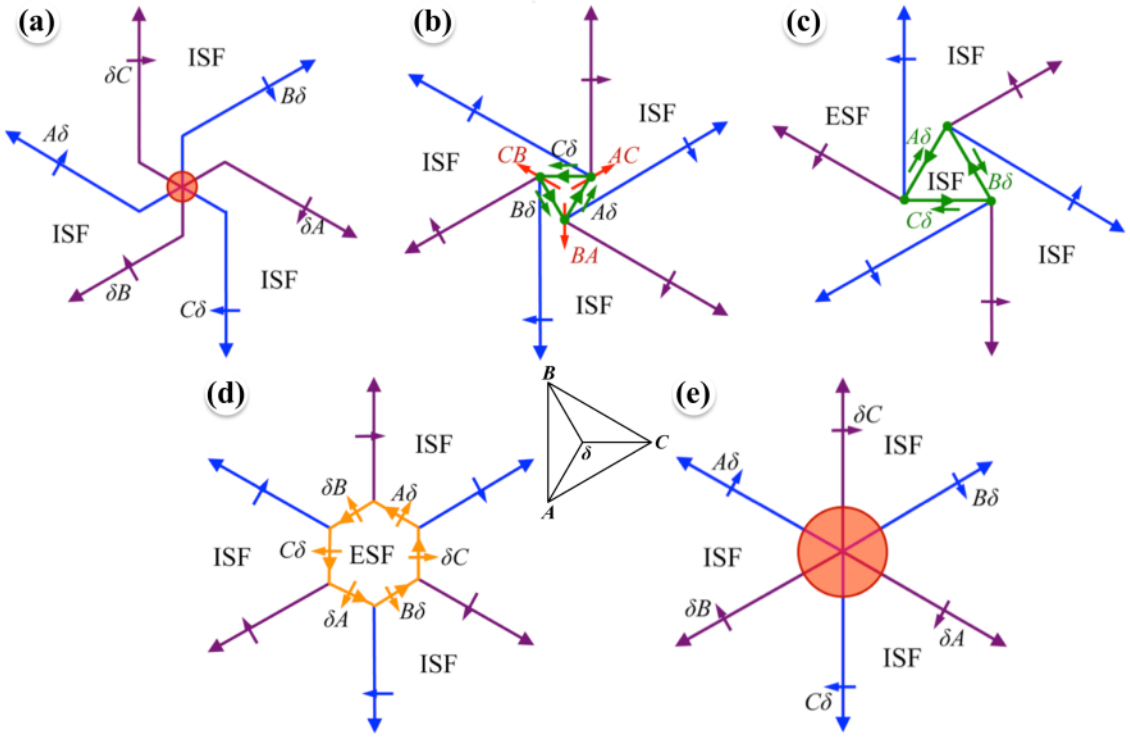

Figure 7. Dislocation structures obtained by disregistry analysis of (a) volume smeared node with spiral dislocation pattern, (b) volume condensed node with "constricted" triangular dislocation pattern, (c) volume condensed node with "expanded" triangular dislocation pattern, (d) volume condensed node with hexagonal dislocation pattern, (e) volume smeared node with straight dislocation pattern.

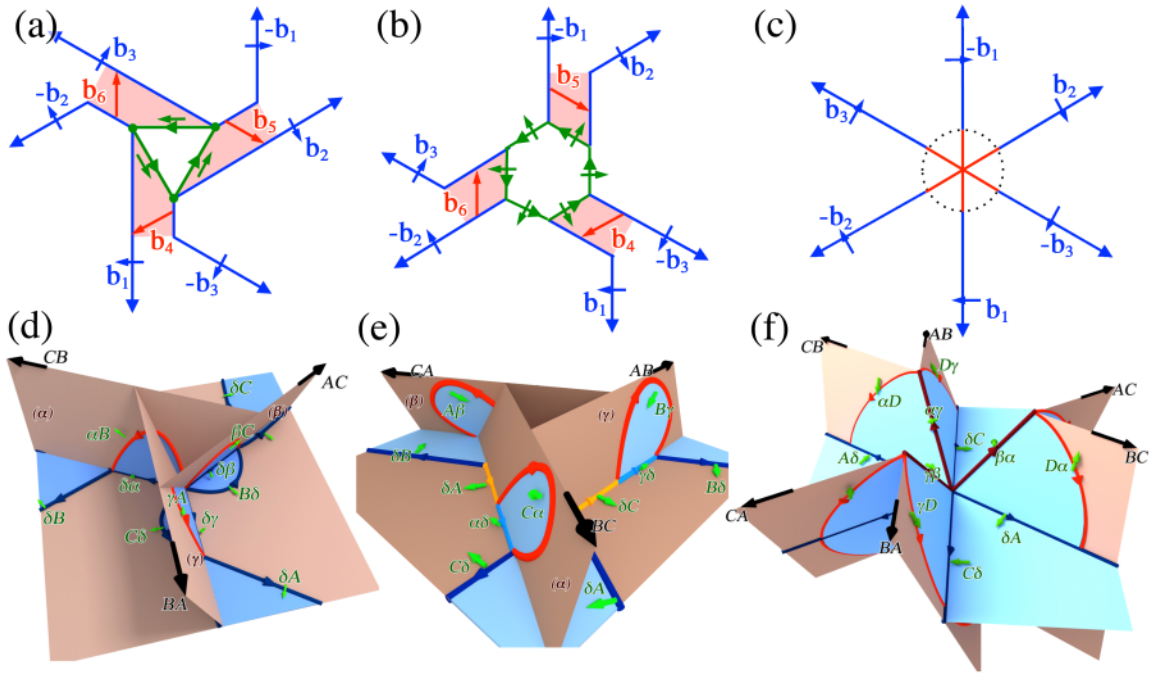

Figure 8. Mechanisms for lattice dislocation nucleation from the volume condensed nodes with triangular (a, d), hexagonal (b, e) and straight (c, f) dislocation patterns. In (a), (b) and (c), the nucleation sites for the lattice dislocations are marked by the red shaded areas and straight red lines. (d), (e), and (f) show the dislocation configuration at nodes after the nucleation of dislocations.

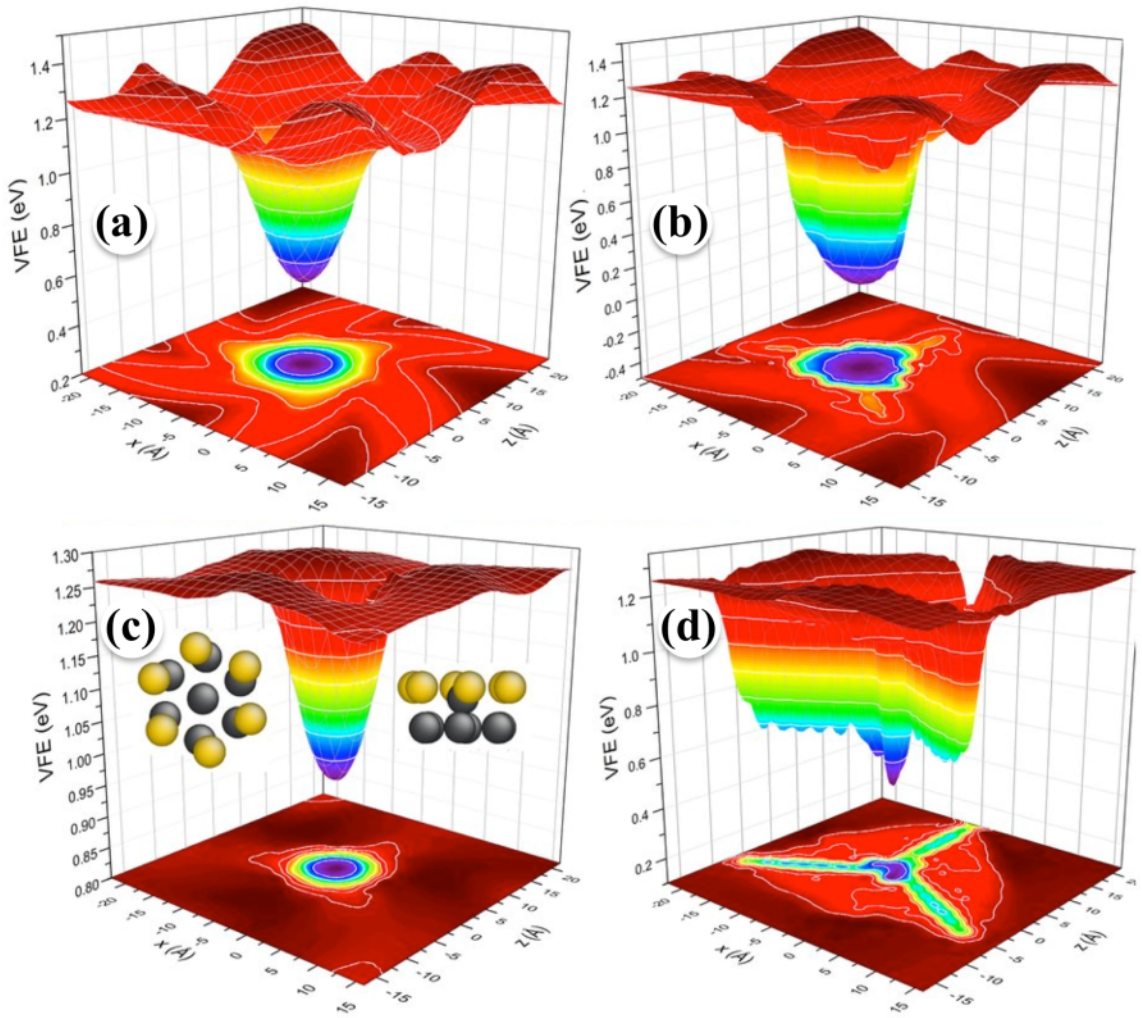

Figure 9. Energy contours of vacancy formation energy in Ni side (a) and Cu side (c) for the volume smeared node with spiral pattern, Cu side (b) and Ni side (d) for the "expanded" node with triangular dislocation pattern.

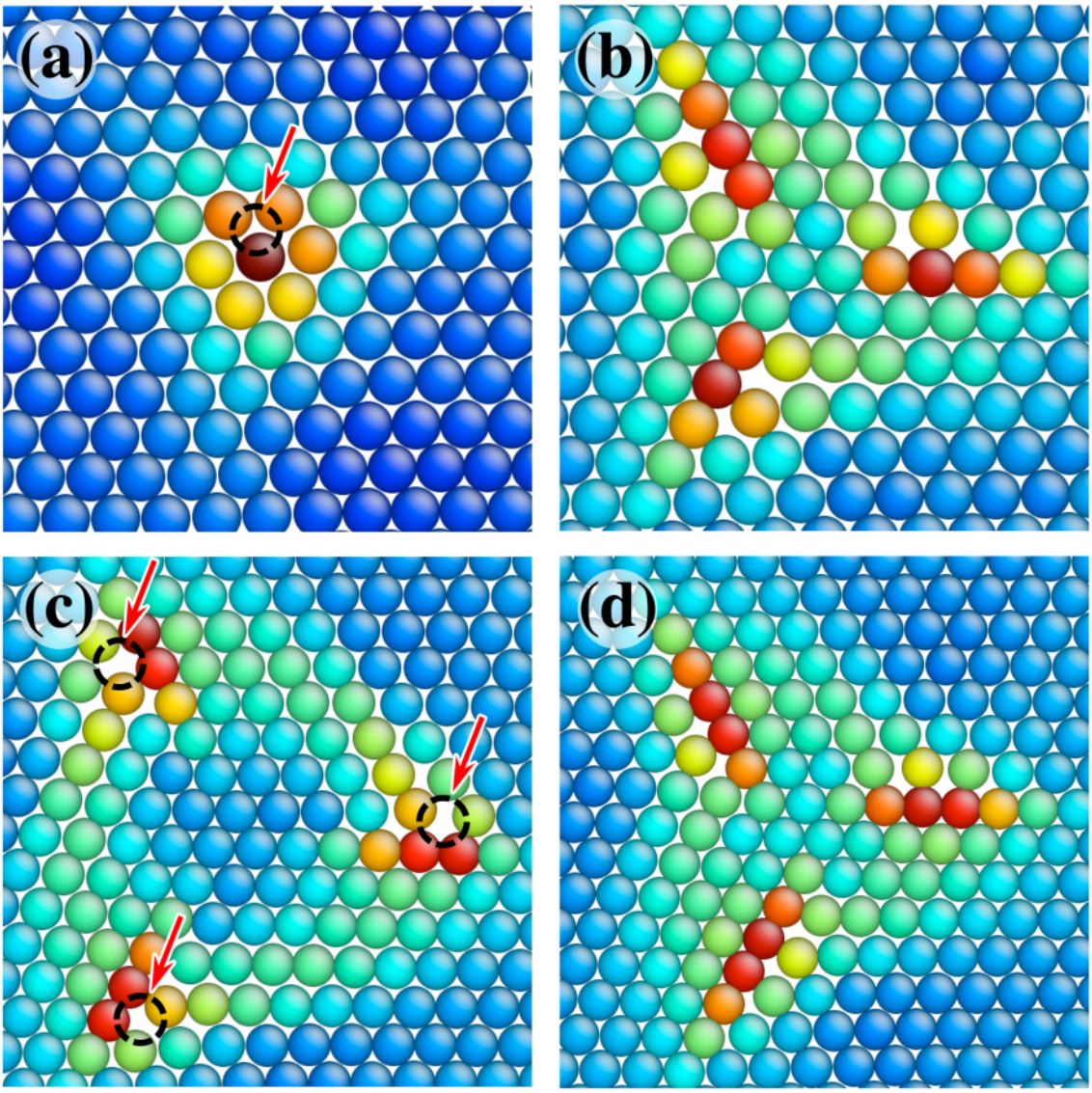

Figure 10. The Structures of self-interstitials at the volume smeared node (a-b) and the volume condensed node with triangular structure (c-d). (a) and (b): the structure of the volume smeared node with spiral pattern before and after the insertion of the interstitial in the dashed black circle. (c) the structure of the volume condensed node with triangular dislocation pattern before and after the insertion of a interstitial at one of the jogs (dashed black circles).

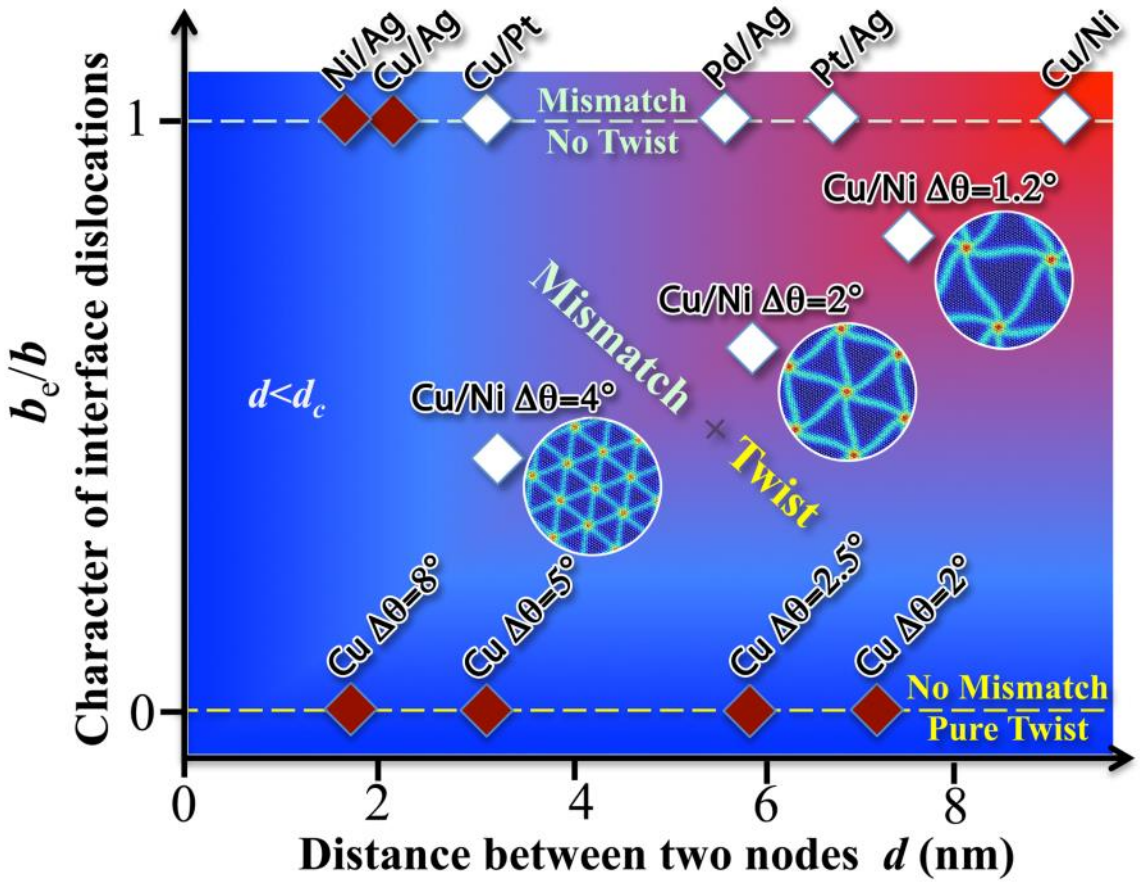

Figure 11. b_e is the edge component of Burgers vector b. The white diamonds indicate the presence of the SP feature in the interface. The brown diamonds indicate the disappearance of the SP feature in the interface. The red region indicates the SP feature in association with both the condensed and the expanded nodes. Blue region indicates the condensed node without the SP feature.